NaCl, $MgCl_2$, and $AlCl_3$ Surface Coverages on Fused Silica and Adsorption Free Energies at pH 4 From Nonlinear Optics

Alyssa L. Olson, Amani O. Alghamdi, and Franz M. Geiger*

Department of Chemistry, Northwestern University,

2145 Sheridan Road, Evanston, IL 60202, USA

Abstract. We employ amplitude- and phase-resolved SHG experiments to probe interactions of fused silica:aqueous interfaces with Al^{3+}, Mg^{2+}, and Na^{+} cations at pH 4 and as a function of metal cation concentration. We quantify the second-order nonlinear susceptibility and the total potential in the presence and absence of 10 mM screening electrolyte to understand the influence of charge screening on cation adsorption. Strong cation:surface interactions are observed in the absence of screen electrolyte. The total potential is then employed to estimate the total number of absorbed cations. The contributions to the total potential from the bound and mobile charge were separated using Gouy-Chapman-Stern model estimates. All three cations bind fully reversibly, indicating physisorption as the mode of interaction. Of the isotherm models tested, the K_d adsorption model fits the data with binding constants of 3 to 30 mol^{-1} and ~300 mol^{-1} for the low (<0.1 mM) and high (0.1 -3 mM) concentration regimes, corresponding to adsorption free energies of -13 to -18 and -24 kJ mol^{-1} at room temperature, respectively. The maximum surface coverages are around 10^{13} cations cm^{-2}, matching the number of deprotonated silanol groups on silica at pH 4. Clear signs of decoupled Stern and diffuse layer nonlinear optical responses are observed and found to be cation specific.

*Corresponding author: f-geiger@northwestern.edu

Introduction. The interaction of inorganic cations with charged aqueous interfaces is important for a variety of settings relevant to environmental chemistry, nanotechnology, energy processes, as well as industrial and engineering applications.[1-2] A major challenge is to quantify the number of adsorbed ions per area under conditions of aqueous flow or as a function of ion concentration, and to assess the extent to which adsorption and desorption are reversible. Of the surface-selective experimental approaches that provide these capabilities, X-ray reflectivity,[3-4] quartz crystal microbalance mass estimates,[5] and nonlinear optical spectroscopy[6-9] are particularly powerful. The latter two techniques circumvent the strong absorber problem of water in the ultraviolet and mid-infrared regions, which prevents the probing of most inorganic ions at surfaces using conventional electronic or vibrational spectroscopic techniques (notable exceptions are oxyanions like arsenate,[10-12] chromate,[13] phosphate,[14] or sulfate.)[15] Interface-specific vibrational spectroscopies such as sum frequency generation probe the response of water's O-H oscillators in the interfacial region to the presence of oxy-[16] and non-oxy ions,[17-21] from which metal cation number densities, or even relative surface coverages, have not yet been quantified due to absorptive-dispersive mixing of the Stern and diffuse layer contributions to the nonlinear optical response.[22-24] Electronic spectroscopies are challenging as most common inorganic ions do not possess strong enough electronic transitions that are readily accessible at buried aqueous interfaces. A notable exception is what has been achieved at the air:water interface using second harmonic generation (SHG) measurements that access solvent to solute charge transfer resonances in the ultraviolet down to 210 nm.[25-27] Electronic resonances involving n-π^* transitions of ions such as nitrate ($\lambda_{max,\,SHG}$=300 nm)[28] or ligand-to-metal charge transfer processes of some select transition metal ions (CrO_4^{2-},

$\lambda_{max, SHG}$=290 nm)[29-34] or uranyl ($\lambda_{max, SHG}$=305-310 nm)[35] at buried aqueous interfaces have also been detected in our laboratory using resonantly enhanced second harmonic generation (SHG).

We recently advanced non-resonant second order nonlinear spectroscopy to probe specific ion interactions at fused silica: aqueous interfaces via the SHG phase and amplitude.[36-43] The approach avoids the strong absorber problem of liquid water and provides the total potential as well as the second order nonlinear susceptibility of buried across interfaces in contact with ions of various chemical identity. We now employ this method to quantify the adsorbed ion density for Al^{3+}, Mg^{2+}, and Na^{+} cations at fused silica surfaces maintained at pH 4 and during exposure to varying concentrations of the metal cation chlorides. Unlike in our recent work, here we work at pH 4, which simplifies the cation speciation so that hydroxides, important for alkaline earths and trivalent cations at elevated pH, are not prevalent.

Experimental. The solutions are prepared using inorganic salts and HCl (Fisher Scientific, ACS Plus, Part # A144, 36.5-38.0%). Stock solutions of 1 M and 10 mM NaCl (Sigma-Aldrich, anhydrous, part # 746398, ≥99% pure)), $MgCl_2$ (from $MgCl_2 \cdot 6H_2O$, Sigma-Aldrich, part # M2670, ≥99.0% pure)), and $AlCl_3$ (from $AlCl_3 \cdot 6H_2O$, Alfa Aesar, part # 10622, 99.9995% pure) were prepared to obtain solutions with concentration ranges between 1 μM to 3 mM. This range was selected because the maximum Al^{3+} concentration that can be used while maintaining a pH of about 4 is 3 mM. 1 M HCl was used to set the pH to 4 as needed. Conductivity (Thermo Scientific, Orion 4-cell I think)and pH (Thermo Scientific, Orion ROSS Ultra Triode, 8107UWMMD)values were determined regularly (Thermo Scientific, Orion Star A325, pH/conductivity meter). Only one salt is tested per day to prevent contamination at the interface from unwanted ions. is tested per day to prevent contamination at the interface from unwanted ions.

We use a 1” diameter fused silica hemisphere (Hyperion Optics, Corning 7979, infrared grade) that is first rinsed in ultrapure water from a Milli-Q system (18.2 MOhm) and then placed in Nochromix solution (*CAUTION: working with Nochromix solution should only be done after reading and understanding the appropriate MSDS sheets*) for at least 1 hour before it is again rinsed with copious amounts of ultrapure water. Then the hemisphere is sonicated in methanol for at least 15 minutes, rinsed, sonicated for 15 minutes, and rinsed again, all with ultrapure water, and then dried using house nitrogen gas passed through a desiccator. The hemisphere is then plasma cleaned (Harrick Plasma) for about 30-60 seconds on "high" setting. The flow cell is then assembled by first dispensing ultrapure water into the flow cell, adding a Viton O-ring, and finally securing the cleaned hemisphere onto the sample cell using clamps.

In the amplitude and phase-resolved laser experiments, the s-polarized 1030 nm output from an amplifier laser system (10 W Pharos, Light Conversion, 200 fs, 200 kHz) is attenuated to 40 mW at the sample, directed onto the silica:water interface using a 100 mm focusing lens while ultrapure water equilibrated in laboratory air overnight (<2 μS cm^{-1}) is flowed through the cell at a rate of 2 mL min^{-1} (Fig. 1A). A peristaltic pump is used to control the flow rate. A 100 mm off-axis parabolic mirror directs the fundamental and the SHG signal from the interface onto a set of optics for time and spatial overlap, and into a photon counter after passing through a short pass filter and a 520 nm bandpass (FWHM=40 nm) filter, as described earlier.[42] Nonlinear optical interference fringes are recorded using a 50 μm thin quartz wafer on a 100 mm motorized translational stage (covering 315.8° of one full period, according to the group velocity dispersion discussed earlier)[42] as a local oscillator source from which the SHG amplitude and phase are determined as detailed in our prior work.[42] After recording a test fringe to ensure accurate

alignment, system is allowed to equilibrate for at least 2 hours while ultrapure water continuously flows through the cell at a rate of 2 mL min^{-1}, after which the SHG phase and amplitude are stable. Then, SHG fringes are collected in fourfold replicates for each solution condition. After each set of four fringes, the next solution is introduced to the system and is flowed for at least 30 minutes at 2 mL min^{-1}. Due to well established hysteresis effects,[40] fringes are recorded in order of increasing ion concentration. For the SHG phase referencing, we use a freshly prepared pH 2.5, 500 mM NaCl aqueous solution each day (*vide infra*).

The SHG intensity measurements employed in our time-dependent experiments are carried out using the same standard sample cell and flow system described above but at a flow rate of 10 mL min^{-1}now the interface is probed by the 1035 nm output of a Light Conversion Flint Oscillator (90 fs pulse duration at 80 MHz repetition rate) attenuated to 0.5 W. We use the p-in/p-out polarization combination and record the SHG intensity using a time resolution of 100 ms. Under these conditions, the fused silica:pH 4 solution interface yields several hundred counts per 100 ms.

Results and Discussion. Fig. 1B shows an example of nonlinear optical interference fringes recorded while flowing ultrapure water first, then an aqueous pH4 solution at $MgCl_2$ concentrations ranging from 1 μM to 1 mM, and finally a pH 2.5 0.5 M salt solution across a fused silica hemisphere. Clear shifts in the fringe amplitude and phase are evident in the data and quantified using a simple cosine fit function of the form $y_0 + E \cdot \cos(\kappa \cdot x + \varphi)$. This equation accounts for the signal offset, y_0, the SHG amplitude, E, and its phase, φ. The constant k =3.14° mm^{-1} arises from all features of our interferometer between the generation of the LO and the signal detection. Like in our earlier work,[42] we reference the SHG phase to the one we obtain at the high

ionic strength and the pH of zero charge (500 mM, pH 2.5), where we expect the surface potential to be minimized and where the SHG response is therefore purely real-valued ($E \propto e^{i\phi}$, where $\phi = 0°$), and the total surface potential, Φ_{tot}, and the nonlinear second order susceptibility, $\chi^{(2)}$, as detailed earlier.[38, 40]

Fig. 2 shows Φ_{tot} and $\chi^{(2)}$ as a function of cation concentration for the three chloride salts we surveyed. When the salts are added with 10 mM screening electrolyte present (Fig. 2A), we find negligible changes in Φ_{tot} and $\chi^{(2)}$, even for the trivalent Al^{3+} cation. This situation is quite different when we perform the adsorption isotherm measurement without any added screening electrolyte (Fig. 2B). Here, we find that the magnitudes of the total potential and the second order nonlinear susceptibility both decrease with increasing metal cation concentration. The decrease is more pronounced for Al^{3+} when compared to Mg^{2+} or Na^{+}. Among all three cations, the sodium cation requires the largest concentration to reduce the magnitude of the total surface potential to a given level, as anticipated given it has the lowest charge density in the series. The nonlinear susceptibility, at a given ion concentration, is smallest for the hardest cation and highest for the softest cation. This result in expected as hyperpolarizabilities, which form the basis for the $c^{(2)}$, tend to increase (*resp.,* decrease) as the polarizability increases (*resp.,* decreases). The nonlinear susceptibility, at a given ion concentration, is smallest for the hardest cation and highest for the softest cation, as perhaps expected from a cation polarizability argument.[44] While a similar trend of decreasing magnitude in F_{tot} and $c^{(2)}$ could be present, we do not have enough statistics within the data to make this claim.

In Fig. 3A we show the adsorbed ion density per square centimeter, N_{ads}, which we compute by first multiplying the difference of the total potential, Φ_{tot}, relative to the lowest metal cation

concentration, $\Phi_{tot,0}$, with the Faraday constant, F, and the cation valency, n,[45-46] then dividing by the thermal energy, RT, and then employing this value as the argument in a Boltzmann term that we multiply into the bulk cation concentration, C_{bulk} with units of mol L^{-1}. Raising this product to the power of 2/3 yields the number of cations per unit area, and a factor of 1/100 converts from decimeters squared to centimeters squared, as shown in the following equation:

$$N_{ads} = C_{bulk} \cdot \left[e^{-n[\Phi_{tot}-\Phi_{tot,0}]F(RT)^{-1}}\right]^{2/3} \cdot 10^{-2} cm^{-2} dm^{-2} \qquad (1)$$

Here, R is the gas constant and T is the temperature (298K). Fig. 3 shows that for all cations we surveyed the surface coverages are quite similar, all the way up to 10^{12} - 10^{13} per square centimeter at the highest concentrations. This saturation level range roughly corresponds to roughly 1% to 10% of the number of silanol groups on fused silica (4.6 x 10^{14} cm^{-2}),[47] or the number of deprotonated silanol groups on a silica surface held at pH 4.[48] The similarity in the overall surface coverages at a given ion concentration seems to indicate that local field effects, such as lateral cation-cation interactions, are not detectable within the uncertainty and intra-sample variation of the data.

Fig. 3B shows the number of adsorbed ions for Na^+ vs Mg^{2+} and Al^{3+} when plotting the x-axis as ionic strength as opposed to cation concentration, signaling a detectable ion specific effect, similar to what is observed in the $\chi^{(2)}$ values shown in Fig. 2B. The Al^{3+} surface coverage at the highest concentration used is in good agreement with results from quartz crystal microbalance measurements reported by the Kabengi group (at 1 mM $Al(NO_3)_3$ and a pH of ~4, a mass of 18 to 19 ng cm^{-2} was detected on silica-terminated sensors, which corresponds to 1.5 x 10^{13} Al^{3+} ions cm^{-2} if all the mass detected is due to the metal cation).[49]

The total potential, Φ_{tot}, contains the contributions from the mobile charges (the anion and cation valency, commonly modeled using Gouy-Chapman and/or Gouy-Chapman-Stern, or GCS, electrical double layer models, or EDLs) as well as from the bound charges (those on the water molecules, the silanol groups, the Si-O-Si bonds, and the ions) that are present in the SHG active region. Subtracting the GCS contribution from Φ_{tot} yields the contribution from the bound charges, according to

$$\Phi(0)_{tot} - \left\{\frac{2k_BT}{ze}\sinh^{-1}\left[\frac{\sigma_{diffuse}}{\sqrt{8k_BT\varepsilon_0\varepsilon_rC}}\right] + \frac{\sigma_{Stern}}{C_{Stern}}\right\} = -\Phi^{non-GCS}_{dipole,quad.\ etc}, \text{ in Volts} \quad (2).$$

Here, z is the ion valence ratio (1:1 for NaCl), C is the ion concentration in the EDL in mol m^{-3}, k_BT is the thermal energy, the σ's are the charge density in the diffuse and Stern layers, *e* is the elementary charge, ε_0 and ε_r are the vacuum permittivity and the relative permittivity of water, respectively, σ_{Stern} and $C_{Stern} = \varepsilon_0\varepsilon_r/d$, are the charge density and capacitance of the Stern layer, respectively, for a given Stern layer thickness, d, and the curly brackets indicate the GCS potential. We can evaluate eqn. 2 by using a Stern layer capacitance of 0.2 F m^{-2} from Sahai and Sverjensky,[50] a Stern layer thickness of 2Å from Brown and co-workers,[51] the ionic strength-dependent interfacial charge densities from Hore and co-workers,[52] and the notion that $|\sigma_{diffuse}|=|\sigma_{Stern}|$ due to charge neutrality in the EDL. Fig. 3C shows that in the ionic strength regime studied here, the GCS potential due to the mobile charges contributes only about 50% of $\Phi(0)_{tot}$ for an aqueous salt solution in contact with fused silica at pH 5.8. For brine conditions, over 90 % of $\Phi(0)_{tot}$ for silica is due to the contribution from the bound charges. In other words, the GCS model recapitulates only 50% (*resp.*, 10%) of the total surface potential at dilute (*resp.*, concentrated) solution conditions. A modified Poisson-Boltzmann model with hydration repulsion[53-54] may provide better agreement between experiment and theory, especially when

further modified with effective ion diameters at charged interfaces,[55] as its good agreement with XPS measurements has been established for silica colloids[53] to account for non-ideal behavior (short-range ion correlations, site availability, etc.) of aqueous electrolytes at surfaces.[55-59] A related issue is the spatial variation of the (field-dependent) relative permittivity, ε_r,[60] which these models neglect, i.e. the solvent is modeled as a uniform continuum, despite large differences in reported ε_r.[50, 55, 61-67] These considerations point to the possibility that the total potential we employ to compute cation surface coverages from eqn. 1 should in fact be reduced by about 50%. Fig. 3D shows the resulting surface coverages, recomputed with eqn. 1 using half of the Φ_{tot} values reported in Fig. 2 (*n.b.*, $\Phi_{tot,0}$ was kept unchanged in this calculation).

Fig. 4 shows fully reversible I_{SHG} vs time traces recorded without phase- or amplitude resolution. This outcome is in good agreement with the Al^{3+} reversibility study (also at pH ~4) published by the Kabengi group.[49] These data indicate that the reversibility condition required for an adsorption isotherm analysis, described further below, is met for all three cations. Fig. 4 also shows the apparent signature of Stern and diffuse layer interactions we reported in 2021 for ionic strength jumps at constant pH.[39] In that work, we found that under certain experimental conditions, the SHG intensity recorded when jumping the ionic strength from 100 mM NaCl to 10 μM NaCl at pH 5.8 undergoes a maximum at early times and then a signal reduction at longer times. Amplitude- and phase-resolved SHG measurements carried out in ~10 sec time resolution led to Φ_{tot}:$\chi^{(2)}$ correlation plots that indicated nonlinear variations of the Stern and diffuse layer nonlinear optical properties. The results provided evidence for structural changes in the Stern and diffuse layers occurring in lockstep under some conditions of changing ionic strength but not others. Fig. 4 appears to indicate that these nonlinear variations of Stern and diffuse layer structure are cation

specific. There appears to be a dependence on flow rate as well, given that the time traces shown in this work were recorded using a flow rate of 10 ml min^{-1}, whereas our previous study was carried out at 5 mL min^{-1} and showed less of a non-monotonic variation in the SHG signal intensity at early times when compared to the present work. These results will be pursued further in upcoming work that is beyond the scope of this study.

Having established that the interaction of our mono-divalent, and trivalent cations with the surface is fully reversible, we proceeded to analyze the adsorption isotherms shown in Fig. 3 using a variety of classical adsorption models.[68-70] Fig. 3 appears to indicate two interaction regimes, one for ion concentrations up to about 0.1 mM and a second regime for higher ion concentrations, as indicated by the dashed lines in Fig. 3A. Attempts to fit a single- or dual-site Langmuir adsorption isotherm model to the data failed, but a dual K_d model[71] of the form $\theta_{ads,i} = K_{d,i} \cdot C_{bulk}$ (here, $\theta_{ads,i}$ is the surface coverage in regime *i* relative to 10^{13} cm^{-2}, the saturation level) resulted in binding constants of 3 to 30 mol^{-1} and ~300 mol^{-1} for the low and high concentration regime, respectively, from which we compute adsorption free energies of -13 to -18 and -24 kJ mol^{-1} at room temperature, respectively (here, we used the 55.5 molarity of liquid water as a standard reference state[72] by which we multiply the binding constants, according to $\Delta G_i = -RT \cdot \ln(55.5 \cdot K_{d,i})$). The range of binding constants and adsorption free energies in the low concentration regime are the result of using eqn. 1 with only 50% of the total potential to account for just the mobile charges (*c.f.* Fig. 3C) as opposed to 100% of the total potential. We can compute associated entropies of adsorption from enthalpy data like those reported by Watts et al. for Na^+ (-405 kJ mol^{-1} on α-quartz at pH 4).[73] While not a one-to-one comparison, our free energy of adsorption and the Watt et al. enthalpy

result in an adsorption entropy of +1.4 kJ mol^{-1} K^{-1}, possibly indicating that the release of Stern layer water molecules, if it occurs upon cation binding, is entropically favorable.

Conclusions. In conclusion, we employed amplitude- and phase-resolved SHG experiments to probe interactions of fused silica:aqueous interfaces with Al^{3+}, Mg^{2+}, and Na^{+} cations at pH 4 and as a function of metal cation concentration. We quantified the second-order nonlinear susceptibility and the total potential in the presence and absence of 10 mM screening electrolyte to understand the influence of charge screening on cation adsorption. Strong cation:surface interactions were observed in the absence of screen electrolyte. The total potential was then employed to estimate the adsorbed ion density for the cations. The contributions to the total potential from the bound and mobile charge were separated using Gouy-Chapman-Stern model estimates. We found that all three cations bind fully reversibly, indicating physisorption as the mode of interaction. Of the isotherm models tested, the K_d adsorption model fit the data with binding constants of 3 to 30 mol^{-1} and ~300 mol^{-1} for the low (<0.1 mM) and high (0.1 -3 mM) concentration regimes, corresponding to adsorption free energies of -13 to -18 and -24 kJ mol^{-1} at room temperature, respectively. The maximum surface coverages are around 10^{13} cations cm^{-2}, matching the number of deprotonated silanol groups on silica at pH 4. Clear signs of decoupled Stern and diffuse layer nonlinear optical responses were observed and found to be cation specific.

Acknowledgements. This work was supported by the US National Science Foundation (CHE-2153191), the Air Force Office of Scientific Research (FA9550-16-1-0379), and the Department of Energy (DE-SC0023342). AA acknowledges a Saudi Aramco Graduate Scholarship. FMG designed the experiment. AA and AO carried out the experiments. AA, AO, and FMG analyzed the data and wrote the manuscript.

References

1. Bañuelos, J. L.; Borguet, E.; Brown Jr, G. E.; Cygan, R. T.; DeYoreo, J. D.; Dove, P. M.; Gaigeot, M.-P.; Geiger, F. M.; Gibbs, J. M.; Grassian, V. H. et al. *Chem. Rev.* **2023,** *123*, 6413-6544.
2. Gonella, G.; Backus, E. H. G.; Nagata, Y.; Bonthuis, D. J.; Loche, P.; Schlaich, A.; Netz, R. R.; Kühnle, A.; McCrum, I. T.; Koper, M. T. M. et al., Water at charged interfaces. *Nature Reviews Chemistry* **2021,** *5* (7), 466-485.
3. Lee, S. S.; Fenter, P.; Nagy, K. L.; Sturchio, N. C., Real-time observation of cation exchange kinetics and dynamics at the muscovite-water interface. *Nature communications* **2017,** *8*, 15826.
4. Bellucci, F.; Lee, S. S.; Kubicki, J. D.; Bandura, A.; Zhang, Z.; Wesolowski, D. J.; Fenter, P., Rb+ Adsorption at the Quartz(101)–Aqueous Interface: Comparison of Resonant Anomalous X-ray Reflectivity with ab Initio Calculations. *The Journal of Physical Chemistry C* **2015,** *119* (9), 4778-4788.
5. Allen, N.; Dai, C.; Hu, Y.; Kubicki, J. D.; Kabengi, N., Adsorption Study of Al3+, Cr3+, and Mn2+ onto Quartz and Corundum using Flow Microcalorimetry, Quartz Crystal Microbalance, and Density Functional Theory. *ACS Earth & Space Chem.* **2019,** *3*, 432-41.
6. Subir, M.; Rao, Y., Environmental Interfacial Spectroscopy. American Chemical Society: 2022.
7. Wen, Y.-C.; Zha, S.; Liu, X.; Yang, S.; Guo, P.; Shi, G.; Fang, H.; Shen, Y. R.; Tian, C., Unveiling Microscopic Structures of Charged Water Interfaces by Surface-Specific Vibrational Spectroscopy. *Physical Review Letters* **2016,** *116* (1), 016101.
8. Lütgebaucks, C.; Gonella, G.; Roke, S., Optical label-free and model-free probe of the surface potential of nanoscale and microscopic objects in aqueous solution. *Phys. Rev. B* **2016,** *94* (19), 195410.
9. Wang, H.-f., Sum frequency generation vibrational spectroscopy (SFG-VS) for complex molecular surfaces and interfaces: Spectral lineshape measurement and analysis plus some controversial issues. *Progress in Surface Science* **2016,** *91*, 155-182.
10. Tofan-Lazar, J.; Al-Abadleh, H. A., ATR-FTIR Studies on the Adsorption/Desorption Kinetics of Dimethylarsinic Acid on Iron-(Oxyhydr)oxides. *Journal of Physical Chemistry A* **2012,** *116* (6), 1596-1604.
11. Adamescu, A.; Hamilton, I. P.; Al-Abadleh, H. A., Thermodynamics of Dimethylarsinic Acid and Arsenate Interactions with Hydrated Iron-(Oxyhydr)oxide Clusters: DFT Calculations. *Environmental Science & Technology* **2011,** *45* (24), 10438-10444.
12. Situm, A.; Rahman, M. A.; Allen, N.; Kabengi, N.; Al-Abadeh, H. A., ATR-FTIR and flow microcalorimetry studies on the initial binding kinetics of arsenicals at the organic–hematite interface. *J. Phys. Chem. A* **2017,** *121*, 5569-79.
13. Kabengi, N.; Chrysochoou, M.; Bompoti, N.; Kubicki, J. J., An integrated flow microcalorimetry, infrared spectroscopy and density functional theory approach to the study of chromate complexation on hematite and ferrihdyrite. *Chem. Geol.* **2017,** *464*, 23-33.
14. Sit, I.; Sagisaka, S.; Grassian, V. H., Nucleotide Adsorption on Iron(III) Oxide Nanoparticle Surfaces:Insights into Nano−Geo−Bio Interactions Through VibrationalSpectroscopy. *Langmuir* **2020,** *36*, 15501-13.

15. Mueller, K.; Lefevre, G., Vibrational Characteristics of Outer-Sphere Surface Complexes: Example of Sulfate Ions Adsorbed onto Metal (Hydr)oxides. *Langmuir* **2011,** *27*, 6830-35.
16. Neal, J. F.; Saha, A.; Zerkle, M. M.; Zhao, W.; Rogers, M. M.; Flood, A. F.; Allen, H., C., Molecular Recognition and Hydration Energy Mismatch Combine To Inform Ion Binding Selectivity at Aqueous Interfaces. *J. Phys. Chem. A* **2020,** *124*, 10171-80.
17. Piontek, S. M.; Borguet, E., Vibrational Dynamics at Aqueous–Mineral Interfaces. *J. Phys. Chem. C* **2022,** *126*, 2307-24.
18. Rehl, B.; Gibbs, J. M., Role of Ions on the Surface-Bound Water Structure at the Silica/Water Interface: Identifying the Spectral Signature of Stability. *J. Phys. Chem. Lett.* **2021,** *12*, 2854-64.
19. DeWalt-Kerian, E. L.; Kim, S.; Azam, M. S.; Zeng, H.; Liu, Q.; Gibbs, J. M., pH-Dependent Inversion of Hofmeister Trends in the Water Structure of the Electrical Double Layer. *J. Phys. Chem. Lett.* **2017,** *8*, 2855-61.
20. Götte, L.; Parry, K. M.; Hua, W.; Verreault, D.; Allen, H. C.; Tobias, D. J., Solvent-Shared Ion Pairs at the Air–Solution Interface of Magnesium Chloride and Sulfate Solutions Revealed by Sum Frequency Spectroscopy and Molecular Dynamics Simulations. *The Journal of Physical Chemistry A* **2017,** *121* (34), 6450-6459.
21. Covert, P. A.; Jena, K. C.; Hore, D. K., Throwing Salt into the Mix: Altering Interfacial Water Structure by Electrolyte Addition. *J. Phys. Chem. Lett.* **2014,** *5*, 143-148.
22. Ohno, P. E.; Wang, H.-f.; Geiger, F. M., Second-order spectral lineshapes from charged interfaces. *Nature communications* **2017,** *8* (1), 1032.
23. Reddy, S. K.; Thiraux, R.; Wellen Rudd, B. A.; Lin, L.; Adel, T.; Joutsuka, T.; Geiger, F. M.; Allen, H. C.; Morita, A.; Paesani, F., Bulk Contributions Modulate the Sum-Frequency Generation Spectra of Water on Model Sea-Spray Aerosols. *Chem* **2018,** *4*, 1629-44.
24. Ohno, P. E.; Wang, H.-f.; Paesani, F.; Skinner, J. L.; Geiger, F. M., Second-Order Vibrational Lineshapes from the Air/Water Interface. *J. Phys. Chem. A* **2018,** *122*, 4457-4464.
25. Petersen, P. B.; Saykally, R. J.; Mucha, M.; Jungwirth, P., Enhanced Concentration of Polarizable Anions at the Liquid Water Surface: SHG Spectroscopy and MD Simulations of Sodium Thiocyanide. *J. Phys. Chem. B.* **2005,** *109*, 10915-10921.
26. Petersen, P. B.; Saykally, R. J., Adsorption of Ions to the Surface of Dilute Electrolyte Solutions: The Jones−Ray Effect Revisited. *J. Am. Chem. Soc.* **2005,** *127*, 15446-15452.
27. Petersen, P. B.; Saykally, R. J., Confirmation of enhanced anion concentration at the liquid water surface. *Chemical Physics Letters* **2004,** *397* (1-3), 51-55.
28. Hayes, P. L.; Malin, J. N.; Konek, C. T.; Geiger, F. M., Interaction of Nitrate, Barium, Strontium and Cadmium Ions with Fused Quartz/Water Interfaces Studied by Second Harmonic Generation *J. Phys. Chem. A* **2008,** *112*, 660-668.
29. Troiano, J. M.; Jordan, D. S.; Hull, C. J.; Geiger, F. A., Interaction of Cr(III) and Cr(VI) with Hematite Studied by Second Harmonic Generation. *J. Phys. Chem. C* **2013,** *117*, 5146-5171.
30. Mifflin, A. L.; Musorrafiti, M. J.; Konek, C. T.; Geiger, F. M., Second Harmonic Generation Phase Measurements of Cr(VI) at a Burried Interface. *J. Phys. Chem. B.* **2005,** *109* (51), 24386-24390.
31. Al-Abadleh, H. A.; Mifflin, A. L.; Musorrafiti, M. J.; Geiger, F. M., Kinetic studies of chromium (VI) binding to carboxylic acid- and methyl ester-functionalized silica/water interfaces important in geochemistry. *Journal of Physical Chemistry B* **2005,** *109* (35), 16852-16859.

32. Al-Abadleh, H. A.; Voges, A. B.; Bertin, P. A.; Nguyen, S. B. T.; Geiger, F. M., Chromium(VI) binding to functionalized silica/water interfaces studied by nonlinear optical spectroscopy. *Journal of the American Chemical Society* **2004,** *126* (36), 11126-11127.
33. Mifflin, A. L.; Gerth, K. A.; Weiss, B. M.; Geiger, F. M., Surface studies of chromate binding to fused quartz/water interfaces. *J. Phys. Chem. A* **2003,** *107* (32), 6212-6217.
34. Mifflin, A. L.; Gerth, K. A.; Geiger, F. M., Kinetics of Chromate Adsorption and Desorption at Fused Quartz/Water Interfaces Studied by Second Harmonic Generation. *J. Phys. Chem. A* **2003,** *107* (45), 9620-9627.
35. Malin, J. N.; Geiger, F. M., Uranyl Adsorption and Speciation at the Fused Silica/Water Interface Studied by Resonantly Enhanced Second Harmonic Generation and the chi(3) Method. *J. Phys. Chem. A* **2010,** *114* (4), 1797-1805.
36. Chang, H.; Lozier, E. H.; Ma, E.; Geiger, F. M., Quantification of Stern Layer Water Molecules, Total Potentials, and Energy Densities at Fused Silica:Water Interfaces for Adsorbed Alkali Chlorides, CTAB, PFOA, and PFAS. *J. Phys. Chem. A* **2023,** *127*, 8404-14.
37. Rehl, B.; Ma, E.; Parshotam, S.; DeWalt-Kerian, E. L.; Liu, T.; Geiger, F. M.; Gibbs, J. M., Water Structure in the Electrical Double Layer and the Contributions to the Total Interfacial Potential at Different Surface Charge Densities. *J. Am. Chem. Soc.* **2022,** *144*, 16338-49.
38. Ma, E.; Ohno, P. E.; Kim, K.; Liu, Y.; Lozier, E. H.; Miller III, T. F.; Wang, H.-f.; Geiger, F. M., A New Imaginary Term in the 2nd Order Nonlinear Susceptibility from Charged Interfaces. *J. Phys. Chem. Lett.* **2021,** *12* (24), 5649-59.
39. Ma, E.; Kim, J.; Chang, H.; Ohno, P. E.; Jodts, R. J.; Miller, T. F.; Geiger, F. M., Stern and Diffuse Layer Interactions during Ionic Strength Cycling. *Journal of Physical Chemistry C* **2021,** *125* (32), 18002-18014.
40. Ma, E.; Geiger, F. M., Divalent Ion Specific Outcomes on Stern Layer Structure and Total Surface Potential at the Silica:Water Interface. *J. Phys. Chem. A* **2021,** *125*, 10079-88.
41. Chang, H.; Ohno, P. E.; Liu, Y.; Lozier, E. H.; Dalchand, N.; Geiger, F. M., Direct Measurement of Charge Reversal on Lipid Bilayers Using Heterodyne-Detected Second Harmonic Generation Spectroscopy. *The Journal of Physical Chemistry B* **2020,** *124* (4), 641-649.
42. Ohno, P. E.; Chang, H.; Spencer, A. P.; Liu, Y.; Boamah, M. D.; Wang, H.-f.; Geiger, F. M., Beyond the Gouy–Chapman Model with Heterodyne-Detected Second Harmonic Generation. *J. Phys. Chem. Lett.* **2019,** *10*, 2328-34.
43. Boamah, M. D.; Ohno, P. E.; Lozier, E.; Van Ardenne, J.; Geiger, F. M., Specifics about Specific Ion Adsorption from Heterodyne-Detected Second Harmonic Generation. *Journal of Physical Chemistry B* **2019,** *123* (27), 5848-5856.
44. Champagne, B., Polarizabilities and hyperpolarizabilities. In *Chemical Modelling: Applications and Theory*, Springborg, M., Ed. Royal Society of Chemistry: 2009; Vol. 6.
45. Peng, M. S.; Duignan, T. T.; Zhao, X. S.; Nguyen, A. V., Surface Potential Explained: A Surfactant Adsorption Model Incorporating Realistic Layer Thickness. *J. Phys. Chem. B* **2020,** *124*, 3195-205.
46. Butt, H. J.; Graf, L.; Kappl, M., *Physics and Chemistry of Interfaces*. 2nd ed.; Wiley-VCH: Weinheim, 2006.
47. Avval, T. C.; Prusa, S.; Cushman, C. V.; Hodges, G. T.; Fearn, S.; Kim, S. H.; Cechal, J.; Vanickova, E.; Babik, P.; Sikola, T. et al., A tag-and-count approach for quantifying surface silanol densities on fused silica based on atomic layer deposition and high-sensitivity low-energy ion scattering. *Appl. Surf. Sci.* **2023,** *607*, 154551.

48. Duval, Y.; Mielczarski, J. A.; Pokrovsky, O. S.; Mielczarski, E.; Ehrhardt, J. J., Evidence of the Existence of Three Types of Species at the Quartz-Aqueous Solution Interface at pH 0-10: XPS Surface Group Quantification and Surface Complexation Modeling. *J. Phys. Chem. B.* **2002,** *106* (11), 2937-2945.
49. Allen, N.; Dai, C.; Hu, Y.; Kubicki, J. D.; Kabengi, N., Adsorption Study of Al3+,Cr3+, and Mn2+onto Quartz and Corundumusing Flow Microcalorimetry, Quartz Crystal Microbalance, andDensity Functional Theory. *ACS Eaarth & Space Chemistry* **2019,** *3*, 432-441.
50. Sahai, N.; Sverjensky, D. A., Evaluation of internally consistent parameters for the triple-layer model by the systematic analysis of oxide surface titration data. *Geochimica Et Cosmochimica Acta* **1997,** *61* (14), 2801-2826.
51. Brown, M. A.; Abbas, Z.; Kleibert, A.; Goel, A.; May, S.; Squires, T. M., Determination of Surface Potential and Electrical Double Layer Structure at the Aqueous Electrolyte-Nanoparticle Interface. *Phys. Rev. X* **2016,** *6* (1), 011007.
52. Jena, K. C.; Covert, P. A.; Hore, D. K., The effect of salt on the water structure at a charged solid surface: differentiating second- and third-order nonlinear contributions. *J. Phys. Chem. Lett.* **2011,** *2*, 1056-1061.
53. Brown, M. A.; Abbas, Z.; Kleibert, A.; Green, R. G.; Goel, A.; May, S.; Squires, T. M., Determination of Surface Potential and Electrical Double-Layer Structure at the Aqueous Electrolyte-Nanoparticle Interface. *Phys. Rev. X* **2016,** *6*, 011007.
54. Brown, M. A.; Bossa, G. V.; May, S., Emergence of a Stern Layer from the Incorporation of Hydration Interactions into the Gouy–Chapman Model of the Electrical Double Layer. *Langmuir* **2015,** *31*, 11477-11483.
55. Pilon, L.; Wang, H.; d''Entremont, A., Recent Advances in Continuum Modeling of Interfacial and Transport Phenomena in Electric Double Layer Capacitors. *J. Electrochem. Soc.* **2015,** *162*, A5158-78.
56. Bazant, M. Z.; Kilic, M. S.; Storey, B. D.; Ajdari, A., Towards an understanding of induced-charge electrokinetics at large applied voltages in concentrated solutions. *J. Coll. Int. Sci.* **2009,** *152*, 48-88.
57. Fedorov, M. V.; Kornyshev, A. A., Ionic liquids at electried interfaces. *Chem. Rev.* **2014,** *114*, 2978-3036.
58. Goodwin, Z. A., .; Feng, G.; Kornyshev, A. A., Mean-Field Theory of Electrical Double Layer In Ionic Liquids with Account of Short- Range Correlations. *Electrochimica Acta* **2017,** *225*, 190-7.
59. Goodwin, Z. A., .; Kornyshev, A. A., Underscreening, Over- screening and Double-Layer Capacitance. *Electrochem. Comm.* **2017,** *82*, 129-33.
60. Becker, M. R.; Loche, P.; Rezaei, M.; Wolde-Kidan, A.; Uematsu, Y.; Netz, R. R.; Bonthuis, D. J., Multiscale Modeling of Aqueous Electric Double Layers. *Chem. Rev.* **2024,** *124*, 1-26.
61. Boamah, M. D.; Ohno, P. E.; Geiger, F. M.; Eisenthal, K. B., Relative Permittivity in the Electrical Double Layer from Nonlinear Optics. *J. Chem. Phys.* **2018,** *148*, 222808.
62. Kurosaki, S., The Dielectric Behavior of Sorbed Water on Silica Gel. *The Journal of Physical Chemistry* **1954,** *58* (4), 320-324.
63. Sakamoto, T.; Nakamura, H.; Uedaira, H.; Wada, A., High-frequency dielectric relaxation of water bound to hydrophilic silica gels. *The Journal of Physical Chemistry* **1989,** *93* (1), 357-366.

64. Wander, M. C. F.; Clark, A. E., Structural and Dielectric Properties of Quartz−Water Interfaces. *The Journal of Physical Chemistry C* **2008,** *112* (50), 19986-19994.
65. Schlaich, A.; Knapp, E. W.; Netz, R. R., Water Dielectric Effects in Planar Confinement. *Physical Review Letters* **2016,** *117* (4), 048001.
66. Teschke, O.; Ceotto, G.; de Souza, E. F., Interfacial water dielectric-permittivity-profile measurements using atomic force microscopy. *Physical Review E* **2001,** *64* (1), 011605.
67. Fumagalli, L.; Esfandiar, A.; Fabregas, R.; Hu, S.; Ares, P.; Janardanan, A.; Yang, Q.; Radha, B.; Taniguchi, T.; Watanabe, K. et al., Anomalously low dielectric constant of confined water. *Science* **2018,** *360*, 1339-42.
68. Langmuir, D., *Aqueous Environmental Geochemistry*. Prentice-Hall, Inc: New Jersey, 1997.
69. Masel, R. I., *Principles of Adsorption and Reaction on Solid Surfaces*. John Wiley & Sons: New York, 1996.
70. Somorjai, G. A., *Chemistry in Two Dimensions*. Cornell University Press: Ithaca, 1981.
71. Volume I: The Kd Model, Methods of Measurement, and Application of Chemical Reaction Codes. In *Understanding Variation in Partiition Coefficient, Kd, Values*, United States Environmental Protection Agency: EPA 402-R-99-004A, 1999.
72. Adamson, A., *Physical Chemistry of Surfaces*. 5th ed ed.; John Wiley & Sons:: New York, 1990.
73. Watts, H. D.; Kubicki, J. D.; Kabengi, N., Connecting Thermodynamics of Alkali Ion Exchange on the Quartz (101) Surface with Density Functional Theory Calculations. *J. Phys. Chem. A* **2022,** *126*, 4286-94.

Figure Captions

Fig. 1. (**A**) Spectrometer used for heterodyne-detected second harmonic generation (HD-SHG). The orange and green pulses represent the 1030 nm fundamental and the 515 nm SHG signal (sig), respectively. LO = local oscillator, SO = short pass filter, BP = bandpass filter, λ/2 = half-wave plate, Pol = polarizer, LP = long pass filter, FL = focusing lens, OAP = off-axis parabolic mirror, TDC = time-delay compensator, and PMT = photomultiplier tube. (**B**) Interference fringes for fused silica surface in contact with ultrapure water (pH 5.8), and 1 μM, 10 μM, 100 μM, and 1 mM of $MgCl_2$, (lightest blue to darkest blue) held at pH 4, and reference solution of pH 2.5 and 500 mM NaCl (green). Vertical dashed lines indicate phase change. 2ω=515 nm.

Fig. 2. (**A**) Nonlinear second-order susceptibility (squares) and the total surface potential (circles) for $MgCl_2$ (gray) and $AlCl_3$ (green) in the presence of 10 mM NaCl screening electrolyte. (**B**) Nonlinear second-order susceptibility (squares) and the total surface potential (circles) for NaCl (green), $MgCl_2$ (gray), and $AlCl_3$ (green) in the absence of 10 mM NaCl screening electrolyte.

Fig. 3. (**A**) Adsorbed ion density as a function of metal cation concentration for Na^+ (green circles), Mg^{2+} (gray circles) and Al^{3+} (empty circles). Dashed lines indicate the two interaction regimes described in the main text. (**B**) Adsorbed ion density as a function of ionic strength for Na^+ (green circles), Mg^{2+} (gray circles) and Al^{3+} (empty circles). (**C**) Total interfacial potential from HD-SHG over fused silica at pH 5.8 and varying ionic strength (white circles) and Gouy-Chapman and GC-Stern model results (solid and dashed lines, all bottom left axis) for various interfacial charge densities, and percent difference in non-GCS potential contribution to total interfacial potential (empty circles, left axis, top). Shading indicates uncertainties; horizontal dashed line indicates 50% level discussed in the main text. (**D**) Adsorbed ion density as a function of ionic strength for Na^+

(green circles), Mg^{2+} (gray circles) and Al^{3+} (empty circles) computed with 50% total interfacial potential. Please see text for detail.

Fig. 4. SHG Intensity vs time traces of fused silica hemispheres in contact with pH 4 aqueous solutions before (<0 min) and during (0 min to 9 min) exposure to 17.7 mM ionic strength solution (17.7 mM NaCl (green), 5.8 mM $MgCl_2$ (dark gray), and 3 mM $AlCl_3$ (light gray)) and during pH 4 flush (>9 min), normalized to the SHG intensity obtained at negative times. 2ω=515 nm.

Fig. 1

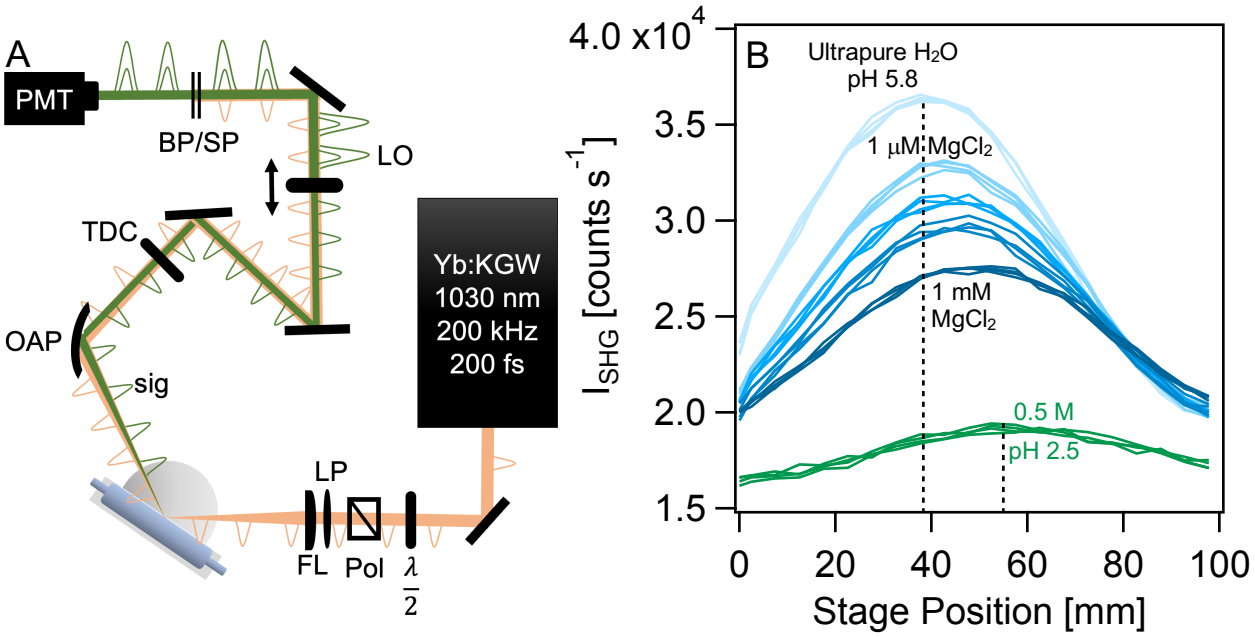
A
PMT
BP/SP
LO
TDC
OAP
sig
Yb:KGW
1030 nm
200 kHz
200 fs
LP
FL
Pol
λ/2
B
Ultrapure H2O
pH 5.8
1 μM MgCl2
1 mM
MgCl2
0.5 M
pH 2.5
4.0 x10^4
3.5
3.0
2.5
2.0
1.5
I_SHG [counts s^-1]
0
20
40
60
80
100
Stage Position [mm]

Fig. 2

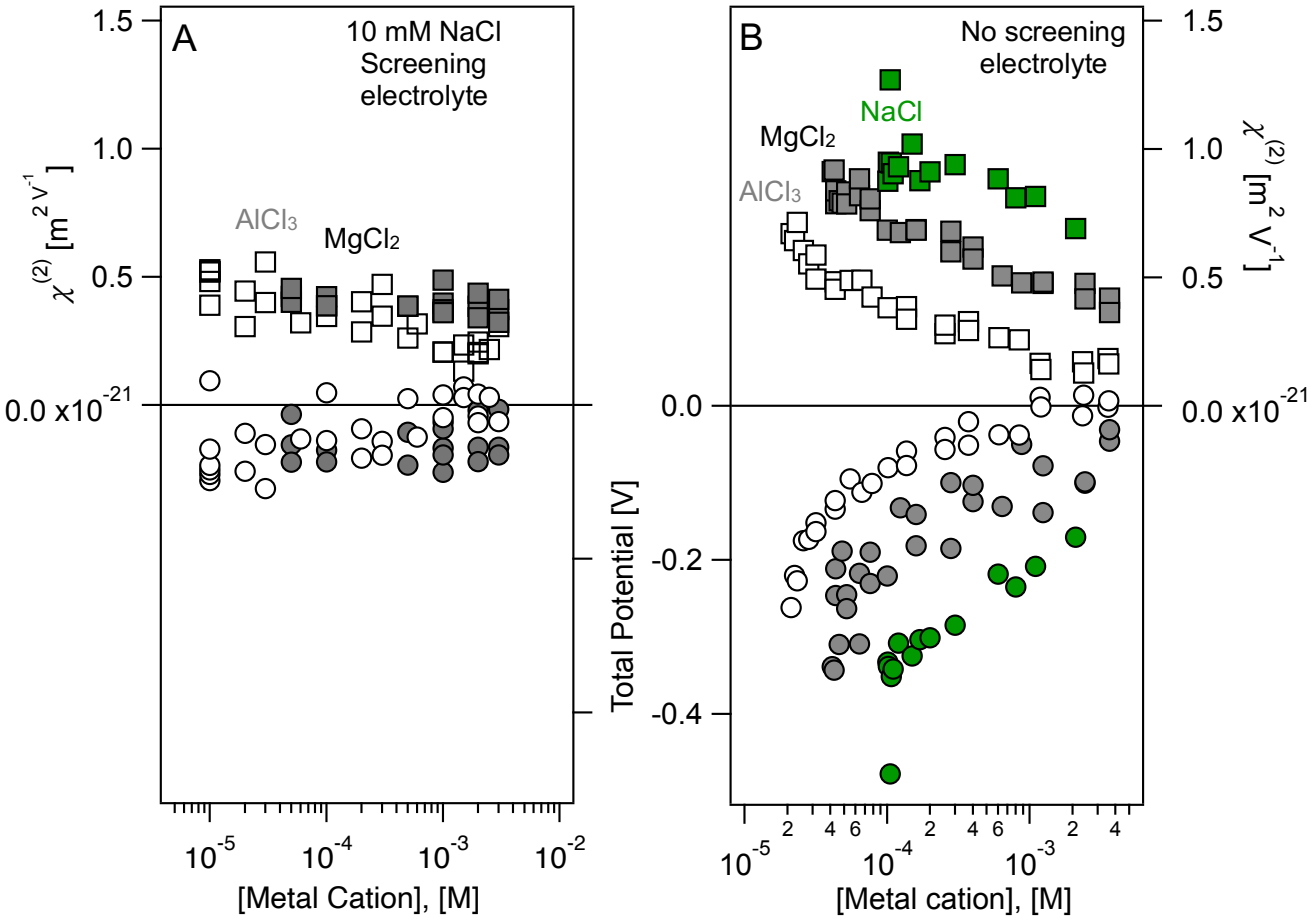
A
10 mM NaCl
Screening
electrolyte
AlCl3
MgCl2
1.5
1.0
0.5
0.0 x10-21
χ(2) [m2 V-1]
10-5
10-4
10-3
10-2
[Metal Cation], [M]
B
No screening
electrolyte
NaCl
MgCl2
AlCl3
0.0
-0.2
-0.4
Total Potential [V]
2 4 6 2 4 6 2 4
[Metal cation], [M]

Fig. 3

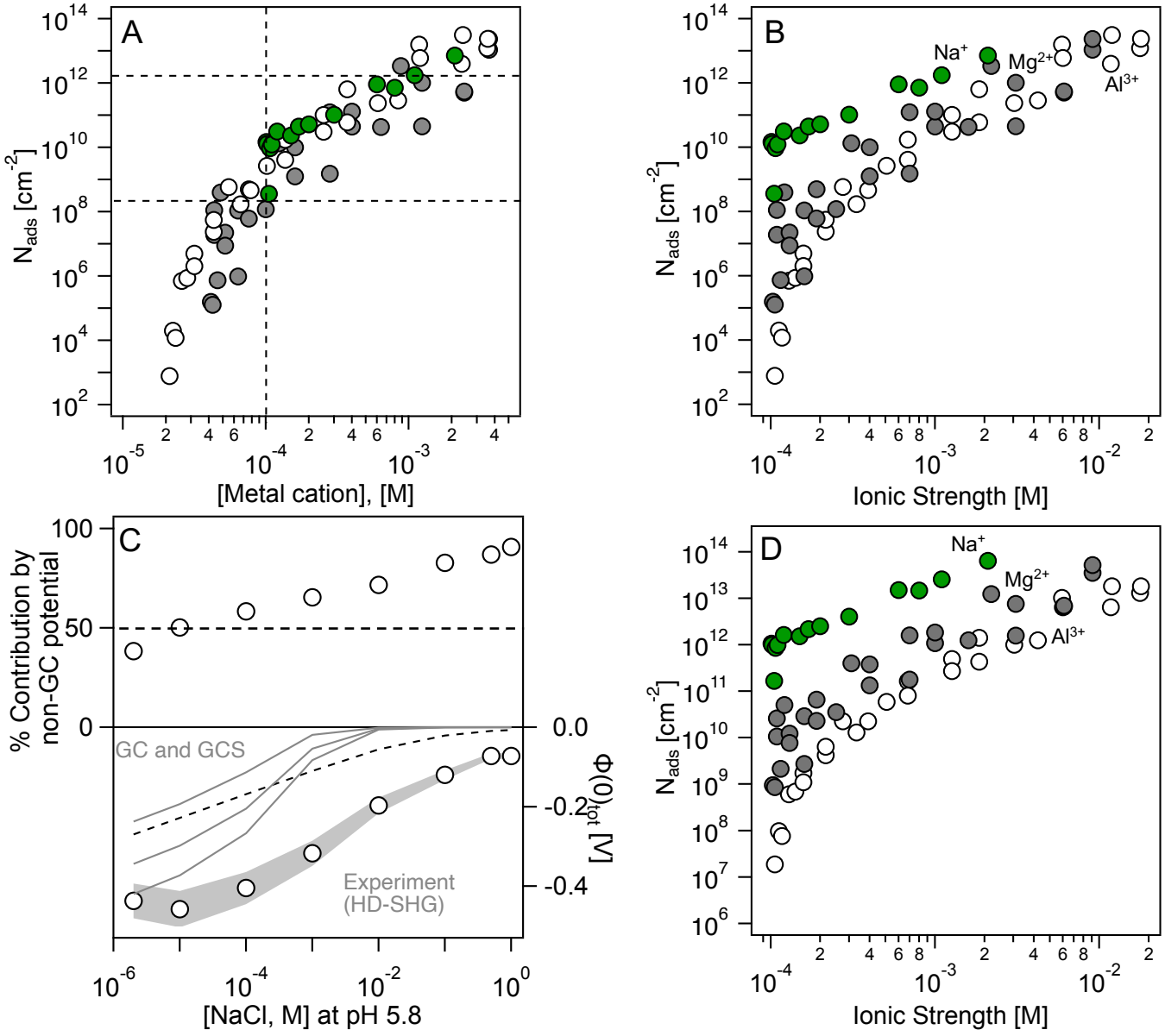
A
N_{ads} [cm^{-2}]
[Metal cation], [M]
B
Na+
Mg2+
Al3+
Ionic Strength [M]
C
% Contribution by non-GC potential
GC and GCS
Experiment (HD-SHG)
$\Phi(0)_{tot}$ [V]
[NaCl, M] at pH 5.8
D
Na+
Mg2+
Al3+
Ionic Strength [M]

Fig. 4

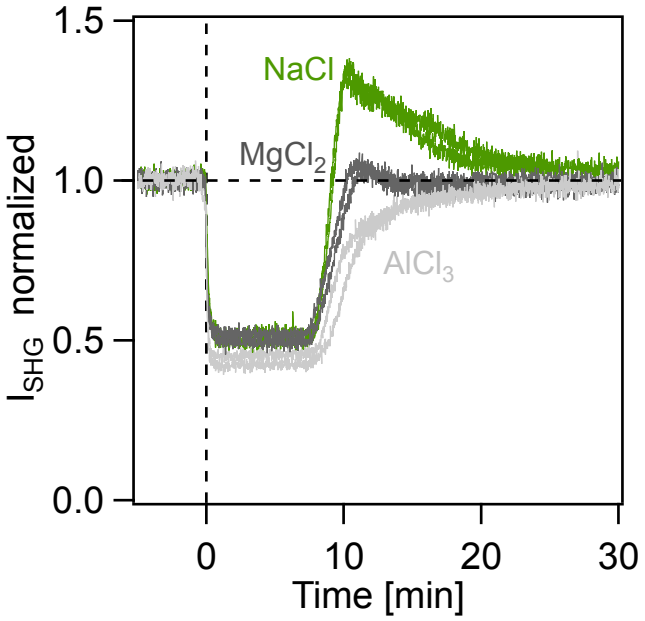
1.5
1.0
0.5
0.0
I_{SHG} normalized
NaCl
$MgCl_2$
$AlCl_3$
0
10
20
30
Time [min]

TOC Graphic